**Astronomy**
**&**
**Astrophysics**

# Dissipative structures of diffuse molecular gas

## I. Broad HCO+ (*J* = 1–0) emission

E. Falgarone[1], G. Pineau des Forêts[2,3], P. Hily-Blant[4], and P. Schilke[5]

[1] LERMA/LRA, CNRS - UMR 8112, École Normale Supérieure, 24 rue Lhomond, 75005 Paris, France
    e-mail: edith.falgarone@lra.ens.fr
[2] IAS, CNRS - UMR 8617, Université Paris-Sud, 91405 Orsay, France
[3] LUTH, CNRS - UMR 8102, Observatoire de Paris, 92195 Meudon, France
[4] IRAM, 300 rue de la Piscine, 38406 St. Martin d'Hères, France
[5] MPIfR, Auf den Hügel 69, 53121 Bonn, Germany

**ABSTRACT**

*Aims.* Specific chemical signatures of the intermittent dissipation of turbulence were sought in diffuse molecular clouds.
*Methods.* We observed HCO+(1−0) lines and the two lowest rotational transitions of $^{12}$CO and $^{13}$CO with an exceptional signal-to-noise ratio in the translucent environment of low-mass dense cores, where turbulence dissipation is expected to take place. Some of the observed positions belong to a new kind of small-scale structure identified in CO(1−0) maps of these environments as the locus of non-Gaussian velocity shears in the statistics of their turbulent velocity field, i.e. singular regions generated by the intermittent dissipation of turbulence.
*Results.* We report the detection of broad HCO+(1−0) lines (10 mK < $T_A^*$ < 0.5 K). We achieve the interpretation of ten HCO+ velocity components by conducting it in conjunction with that of the associated optically thin $^{13}$CO emission. The derived HCO+ column densities span a broad range, $10^{11} < N(\text{HCO}^+)/\Delta v < 4 \times 10^{12}$ cm$^{-2}$/km s$^{-1}$, and the inferred HCO+ abundances, $2 \times 10^{-10} < X(\text{HCO}^+) < 10^{-8}$, are more than one order of magnitude above those produced by steady-state chemistry in gas that is weakly shielded from UV photons, even at large densities. We compare our results with predictions of non-equilibrium chemistry, swiftly triggered in bursts of turbulence dissipation and followed by a slow thermal and chemical relaxation phase, assumed to be isobaric. The set of values derived from observations, i.e. large HCO+ abundances, temperatures in the range of 100−200 K, and densities in the range 100–$10^3$ cm$^{-3}$, unambiguously belongs to the relaxation phase. In contrast, the kinematic properties of the gas suggest that the observed HCO+ line emission results from a space-time average in the beam of the whole cycle followed by the gas and that the chemical enrichment is made at the expense of the non-thermal energy. Last, we show that the "warm chemistry" signature (i.e. large abundances of HCO+, CH+, H$_2$O, and OH) acquired by the gas within a few hundred years, which is the duration of the impulsive chemical enrichment, is kept over more than a thousand years. During the relaxation phase, the H$_2$O/OH abundance ratio stays close to the value measured in diffuse gas by the SWAS satellite, while the OH/HCO+ ratio increases by more than one order of magnitude.

**Key words.** astrochemistry – turbulence – ISM: molecules – ISM: structure – ISM: kinematics and dynamics – radio lines: ISM

## 1. Introduction

Parsec scale maps of molecular clouds with only moderate star formation provide a comprehensive view of the environment of dense cores before their disruption by young star activity. Whether the tracer is extinction, molecular lines or dust thermal emission, large scale maps reveal long and massive filaments of gas and dust. Dense cores are most often nested in these filaments, which are presumably their site of formation. The open questions raised by star formation thus include those on dense core and filament formation. As filaments are in essence structures that are at least one order of magnitude longer than they are thick, their observational study requires maps with a wide dynamic range. These observations, now available, open new perspectives: filaments are ubiquitous and span a broad range of mass per unit length, from massive filaments (Abergel et al. 1994; Mizuno et al. 1995; Haikala et al. 2004) to most tenuous (Hily-Blant 2004; Falgarone et al. 1991, 2001).

Recent observations of the environment of low mass dense cores in $^{12}$CO and $^{13}$CO rotational transitions have also brought to light previously hidden velocity structures. The turbulent velocity field of core environments, like turbulent gas, exhibits more large velocity shears at small scale than anticipated from a Gaussian distribution, and the spatial distribution of the non-Gaussian occurrences of velocity shears delineates a new kind of small scale structure in these core environments. Their locus forms a network of narrow filaments, not coinciding with those of dense gas (Pety & Falgarone 2003; Hily-Blant 2004; Hily-Blant et al. 2006). It has been shown by Lis et al. (1996) that they trace the extrema of the vorticity projected in the plane of the sky. As discussed in Pety & Falgarone (2003), these velocity structures of large vorticity probably trace either fossil shocks that have generated long-lived vorticity, or genuine coherent[1]

---

[1] So-called because their lifetime is significantly longer than their period.

vortices, both manifestations of the intermittency of turbulence dissipation (Pety & Falgarone 2000).

Interestingly, these structures might be the long-sought sites of turbulence dissipation in molecular clouds, as proposed by (Joulain et al. 1998, hereafter JFPF), and thus the sites of the elusive warm chemistry put forward to explain the large abundances of CH$^+$ (e.g., Crane et al. 1995; Gredel et al. 2002; Gredel 1997), HCO$^+$ (Lucas & Liszt 1996, 2000), and now H$_2$O (Neufeld et al. 2002; Plume et al. 2004) observed in diffuse molecular clouds. Since all the above observations are absorption measurements in the submillimeter, radio, and visible domains, they suffer from line-of-sight averaging restricted to specific directions and from a lack of spatial information regarding the actual drivers of this "warm chemistry".

The present work is the first attempt at detecting the chemical signatures of locations identified in nearby clouds as the possible sites of the "warm chemistry" in diffuse molecular clouds, i.e. the locus of the enhanced dissipation of supersonic turbulence. It is part of a series of papers dedicated (i) to the properties of this new kind of filament in dense core environments, with the broad perspective of understanding how non-thermal turbulent energy is eventually converted and lost as dense filaments and cores form; and (ii) to the timescales and spatial scales involved in the non-linear thermal and to chemical evolution of the dissipative structures of turbulence.

Unfortunately, dissipative structures have a small volume filling factor at any time. They are difficult to characterize because their emission is weak in most tracers. A multi-transition analysis of CO observations, up to the $J$=4–3 transition, provides a full range of temperatures and densities for this gas, ranging from 20 K and $10^4$ cm$^{-3}$ to 200 K and 100 cm$^{-3}$ (Falgarone & Phillips 1996). Recent observations in the two lowest rotational lines of $^{12}$CO and $^{13}$CO show that the gas there is associated spatially, although not coincident, with gas that is optically thin in the $^{12}$CO(1−0) line (Hily-Blant 2004; Hily-Blant & Falgarone 2006).

The present paper reports observations and analysis of the HCO$^+$(1−0) emission of a few such structures previously identified in nearby molecular clouds. Each of them is characterized by a different value of the local velocity shear measured in the $^{12}$CO lines in order to sample different strengths (or stages) of the dissipation process. In a companion paper, we present the substructure in one of these filaments as detected in a mosaic of 13 fields mapped in the $^{12}$CO(1−0) line with the Plateau de Bure Interferometer (PdBI) (Falgarone et al. 2006). The target fields and the observations are described in Sect. 2. We explain the line analysis carried out to derive molecular abundances in Sect. 3. In Sect. 4, we show that they cannot be reconciled with current models of steady-state chemistry and that an alternative model involving non-equilibrium heating and chemistry reasonably reproduces the main features of our data, although this model is by no means final. The discussion in Sect. 5 is devoted to the limitations of our study and the implications of the interpretation we propose.

## 2. Observations

### 2.1. The target fields

The selected targets belong to the environments of the dense cores studied by Falgarone et al. (1998) and Pety & Falgarone (2003). These cores were selected because of their particularly transparent environment that helps isolate the gas directly connected to the cores and minimizes confusion with unrelated

components. One is located in the Polaris Flare, a high-latitude cloud (Heithausen et al. 2002), and is embedded in an environment where the visual extinction derived from star counts at high angular resolution (<1 arcmin) is $0.6 < A_V < 0.8$ mag (Cambrésy et al. 2001). The other, L1512 (Lee et al. 2001), is located at the edge of the Taurus-Auriga-Perseus complex in a region of low average column density at the parsec scale ($N_{H_2}$ of a few $10^{20}$ cm$^{-2}$, as deduced from the low angular resolution $^{12}$CO($J$=1−0) observations of Ungerechts & Thaddeus (1987). L1512 appears to be a very young dense core because it is one of the least centrally condensed of the nearby dense cores mapped in the submillimeter emission (Ward-Thompson et al. 1994) and has no signpost of infall motions toward a central object, such as the so-called blue-line asymmetry (Gregersen & Evans 2000). It is also one of the dense cores where the observed molecular linewidths are the narrowest, yet not purely thermal (Fuller & Myers 1993).

Four positions were observed in the Polaris environment and one in that of L1512. They are shown in the $^{12}$CO($J$=2−1) channel maps of Figs. 1 and 2 from the IRAM-30 m data of Falgarone et al. (1998). These positions sample the full range of small scale velocity shears, following the statistics of the velocity field of Pety & Falgarone (2003). The observed quantity used in such statistics is the $^{12}$CO line centroid velocity increment (CVI) measured for a given lag. The CVI values measured for a lag of 0.02 pc are given in Table 1 for each position. They correspond to local velocity shears (in the plane of the sky) ranging from 3 to 20 km s$^{-1}$ pc$^{-1}$, the lowest value in the Polaris field belonging to the Gaussian core of the probability distribution of the CVIs in that field, while the highest values (positions #2 and #3 in Polaris) belong to its non-Gaussian tails. The CVI value in L1512 also belongs to the non-Gaussian tail of the CVI probability distribution, but is close to the limit of its Gaussian core.

### 2.2. Observations and results

The observations were carried out at the IRAM-30 m telescope and spread over three summer sessions (1996, 1998 and 1999). A few additional $^{12}$CO and $^{13}$CO($J$=2−1) lines were obtained in the framework of another project during a winter session in 1999. The weather conditions never allowed us to observe at high frequency during the summers and the lines observed were HCO$^+$($J$=1−0), $^{13}$CO($J$=1−0), and C$_2$H(3/2−1/2). Frequency switching by 7.8 MHz was used to subtract the off-line emission. The autocorrelator had a resolution of 20 kHz, providing a velocity resolution of 0.08 km s$^{-1}$ at 89 GHz. The single sideband (SSB) noise temperatures of the receivers greatly improved in 1999 when a new generation of receivers was installed. At 3 mm, the SSB receiver temperatures were in the range 80−130 K depending on the frequency before 1999 and 50−65 K in 1999. The system temperatures were in the range 200−250 K before 1999 and between 150 and 250 K in 1999. The sideband rejections were estimated to be about 20 dB. At 230 GHz, the SSB receiver temperature was about 90 K with ≈13 dB gain rejection. The HCO$^+$($J$=1−0), $^{13}$CO($J$=1−0), and $^{12}$CO($J$=2−1) line profiles are shown in Figs. 3−6 for the five positions, along with a unique C$_2$H spectrum.

In L1512, the line of sight crosses the dense core, so the spectra comprise the emission of both the dense core (the narrow component between 7.1 and 7.3 km s$^{-1}$) and that of its environment extending from 6.4 to 8.2 km s$^{-1}$. This velocity interval is assigned to the environment of the core on the basis of the line profile properties and of the large scale channel maps of
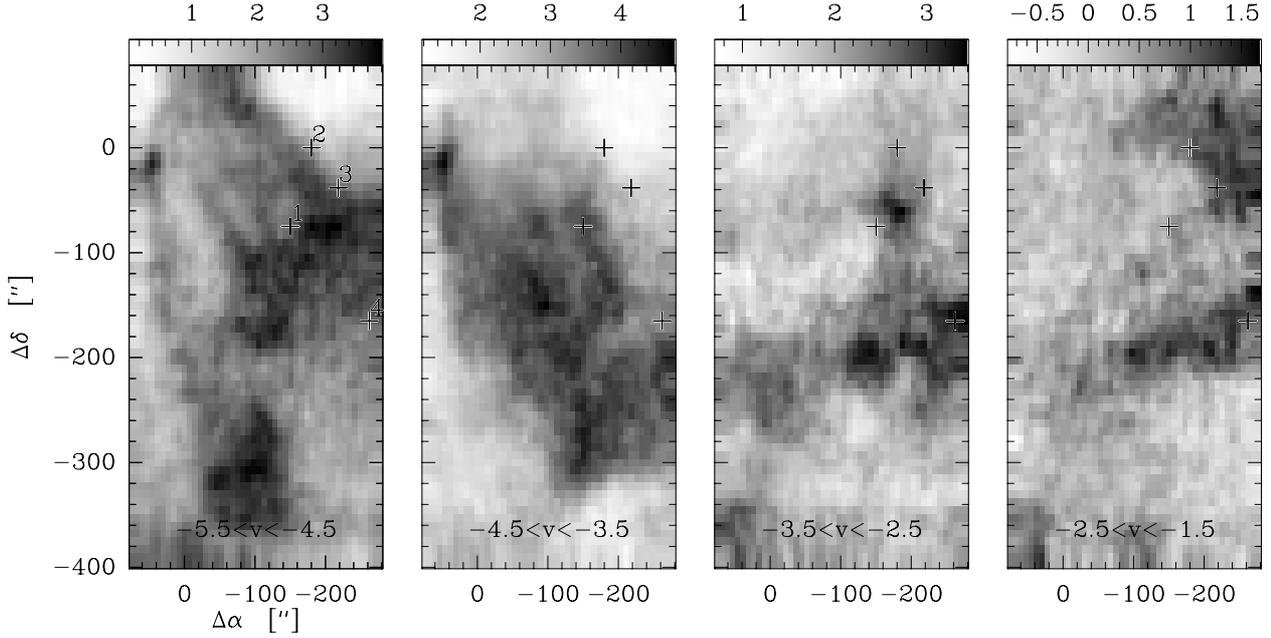
**Fig. 1.** $^{12}$CO($J$=2−1) channel maps of the Polaris field. The 4 positions observed in HCO$^+$ lie at offsets (−150″, −75″), (−180″, 0), (−218″, −38″), (−262″, −165″) relative to (0, 0): $l_{II}$ = 123.68, $b_{II}$ = 24.93. They are indicated with crosses (positions 1 through 4, respectively). The dense core, not visible in the $^{12}$CO lines, is located along the eastern edge of the map, south of offset (0, 0). The velocity intervals in km s$^{-1}$ are given at the bottom of each panel.
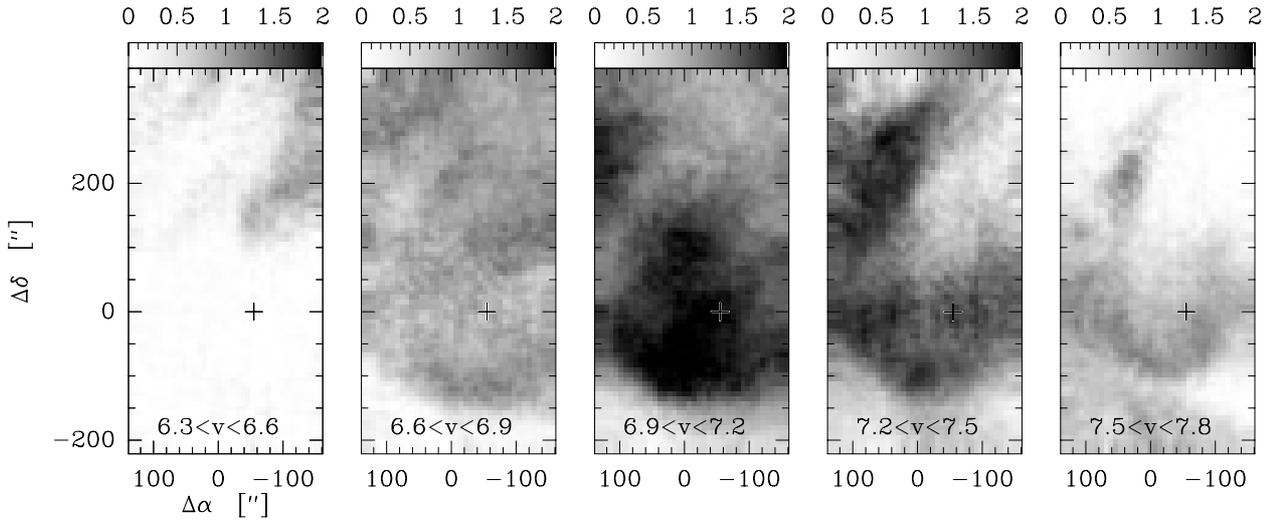


**Fig. 2.** $^{12}$CO($J$=2−1) channel maps of the L1512 field. The position observed in HCO$^+$ is at offset (−55″, 0) relative to (0, 0): RA = 05$^h$00$^m$54.5$^s$, Dec = 32°39′ (1950). The dense core is centered on the (0, 0) position and is about 2 arcmin in diameter (Lee et al. 2001; Pety & Falgarone 2003). The velocity intervals in km s$^{-1}$ are given at the bottom of each panel.

Falgarone et al. (1998) and Falgarone et al. (2001). In Polaris, the lines of sight do not intercept the dense core, so the observed emission is from the environment exclusively.

The exceptional signal-to-noise ratio of the line profiles reveals a wide variety of complex non-Gaussian line profiles, with several broad and weak components. There is general agreement between the total velocity extent of the CO and HCO$^+$ lines (except for position #4 in Polaris), but the line-shapes are all extremely different. The velocity components visible in the $^{13}$CO spectra are most often present in the HCO$^+$ spectra at the same position. The HCO$^+$ and $^{13}$CO lines have thus been decomposed into several Gaussians with the goal of ascribing a $^{13}$CO(1−0) counterpart to each of the HCO$^+$ components. The decomposition of these profiles into Gaussians is not

straightforward, and certainly not unique, but it offers guidance in analyzing the spectra. Yet, as shown in Table 1, not all the components found in the Gaussian fitting procedure of the HCO$^+$ lines were successfully found in that of the $^{13}$CO lines and vice versa. In most cases, the broad HCO$^+$ weak emission was fitted with a single Gaussian, although in a few cases, several narrower Gaussians would also fit the profile.

We restricted our analysis of the HCO$^+$ lines to those components that are visible in the $^{13}$CO(1−0) spectra i.e. those for which a $^{13}$CO counterpart exists with comparable centroid velocity and width. They are labelled with letters in Table 1. Instead of analyzing all the profiles separately, we give outlines of the solutions by splitting the range of line temperatures into five cases (labelled by letters A to E). Each case is identified by

**Table 1.** HCO$^+$($J$=1−0), $^{13}$CO($J$=1−0), and C$_2$H(3/2−1/2) line properties derived from Gaussian decompositions. In several cases, velocity components with similar centroid and width appear in the HCO$^+$ and $^{13}$CO spectra. They are labelled A, B, C, D, or E depending on the strength of the lines. These are the five cases for which the analysis can be completed. The rms noise level $\sigma$ of the spectra is also given. The value of the centroid velocity increment (CVI) measured over a lag of 0.02 pc on the $^{12}$CO(1−0) line at each position is also given.

| | offsets | | CVI | | HCO$^+$($J$=1−0) | | | | $^{13}$CO($J$=1−0) | | | |
|---|---|---|---|---|---|---|---|---|---|---|---|---|
| | ″ | ″ | km s$^{-1}$ | | $v_i$ km s$^{-1}$ | $T^*_{Ai}$ K | $\sigma$ mK | $\Delta v_i$ km s$^{-1}$ | $v_i$ km s$^{-1}$ | $T^*_{Ai}$ K | $\sigma$ mK | $\Delta v_i$ km s$^{-1}$ |
| Polaris #1 | −150 | −75 | 0.08 | D | −4.7 | 0.15 | 5 | 0.65 | −4.7 | 2. | 16 | 0.4 |
| | | | | D | −4.3 | 0.12 | | 0.6 | −4.3 | 2.2 | | 0.5 |
| | | | | C | −3.6 | 0.02 | | 0.4 | −3.8 | 0.8 | | 0.3 |
| | | | | A | −2.7 | 0.015 | | 1.1 | −3.4 | 0.14 | | 1.1 |
| Polaris #2 | −180 | 0 | 0.4 | C | −4.8 | 0.06 | 3 | 0.4 | −4.6 | 0.6 | 11 | 0.5 |
| | | | | | −4.55 | 0.08 | | 0.5 | −3.3 | 0.2 | | 0.8 |
| | | | | B | −3.9 | 0.02 | | 1.2 | −2.9 | 0.2 | | 0.8 |
| | | | | A | −2.9 | 0.01 | | 2.0 | −3.0 | 0.07 | | 2.1 |
| Polaris #3 | −218 | −38 | 0.4 | C | −4.7 | 0.075 | 3 | 0.7 | −4.7 | 1.5 | 6 | 0.5 |
| | | | | B | −4.0 | 0.03 | | 1.1 | −3.4 | 0.3 | | 1.2 |
| | | | | A | −2.5 | 0.01 | | 1.8 | −1.9 | 0.09 | | 0.9 |
| Polaris #4 | −262 | −165 | 0.1 | C | −4.6 | 0.05 | 8 | 1.0 | −4.5 | 0.7 | 24 | 1.2 |
| | | | | C | −3.6 | 0.06 | | 1.3 | −3.9 | 1.4 | | 1.2 |
| | | | | C | −3.2 | 0.07 | | 0.4 | −3.2 | 0.9 | | 0.5 |
| | | | | | | | | | −2.8 | 0.08 | | 2.4 |
| L1512 | −55 | 0 | 0.06 | E | 7.0 | 0.5 | 6 | 0.3 | 7.0 | 3.7 | 50 | 0.2 |
| | | | | dc | 7.2 | 1.7 | | 0.15 | 7.2 | 4.4 | | 0.3 |
| | | | | C | 7.2 | 0.05 | | 0.9 | 7.4 | 1.3 | | 0.6 |

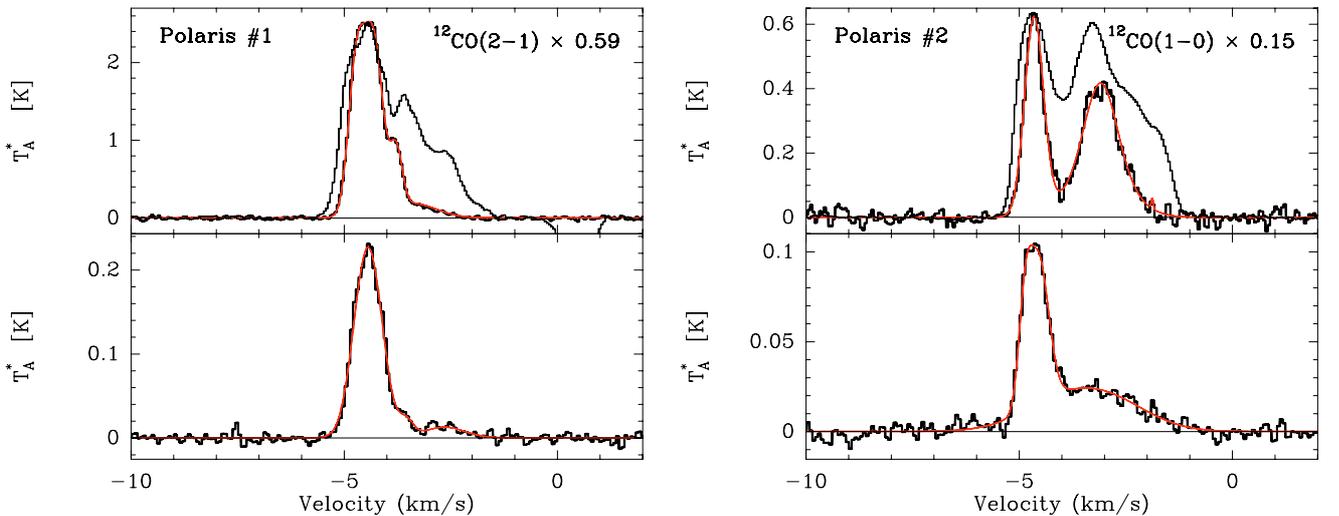| | offsets | | C$_2$H(3/2, 2−1/2, 1) | | | |
|---|---|---|---|---|---|---|
| | ″ | ″ | $v_i$ km s$^{-1}$ | $T^*_{Ai}$ mK | $\sigma$ mK | $\Delta v_i$ km s$^{-1}$ |
| Polaris #2 | −180 | 0 | −3.5 | 7. | 3. | 3.0 |



**Fig. 3.** In each of the 4 panels, corresponding to the 4 positions observed in the Polaris field, three lines are displayed: $^{13}$CO($J$=1−0) (thick line) and a multi-component Gaussian fit (thick red curve), $^{12}$CO (either ($J$=1−0) or ($J$=2−1), as indicated) multiplied to fit the $^{13}$CO temperature scale, and the HCO$^+$($J$=1−0) at the bottom with a multi-component Gaussian fit (thick red curve).

its HCO$^+$(1−0) temperature within a factor on the order of 3, given in Table 2. Note that in all cases but E, the HCO$^+$/$^{13}$CO line temperature ratio is ≈0.1. The weakest cases are the A's, while the E case approaches the conditions within dense cores (noted "dc" in Table 1). The characteristics of all the components are reported in Table 1, which shows that the HCO$^+$ line temperatures range between 0.01 and 0.5 K, a range similar to that found towards $\zeta$ Oph by Liszt & Lucas (1994) and in the direction of several extragalactic sources by Lucas & Liszt (1996). An interesting rough anticorrelation appears between the HCO$^+$ peak intensity and the width of each component where

approximately $T^*_{Ai}$(HCO$^+$) $\propto \Delta v_i^{-2}$ (Fig. 7). It will be discussed in Sect. 4.5.

## 3. Column densities and abundances

### 3.1. HCO$^+$

HCO$^+$ line intensities were interpreted in the framework of the large velocity gradient (LVG) formalism. The collisional excitation due to electrons has been included in the code following Bhattacharyya et al. (1981), with ionization degrees $x_e = 10^{-4}$
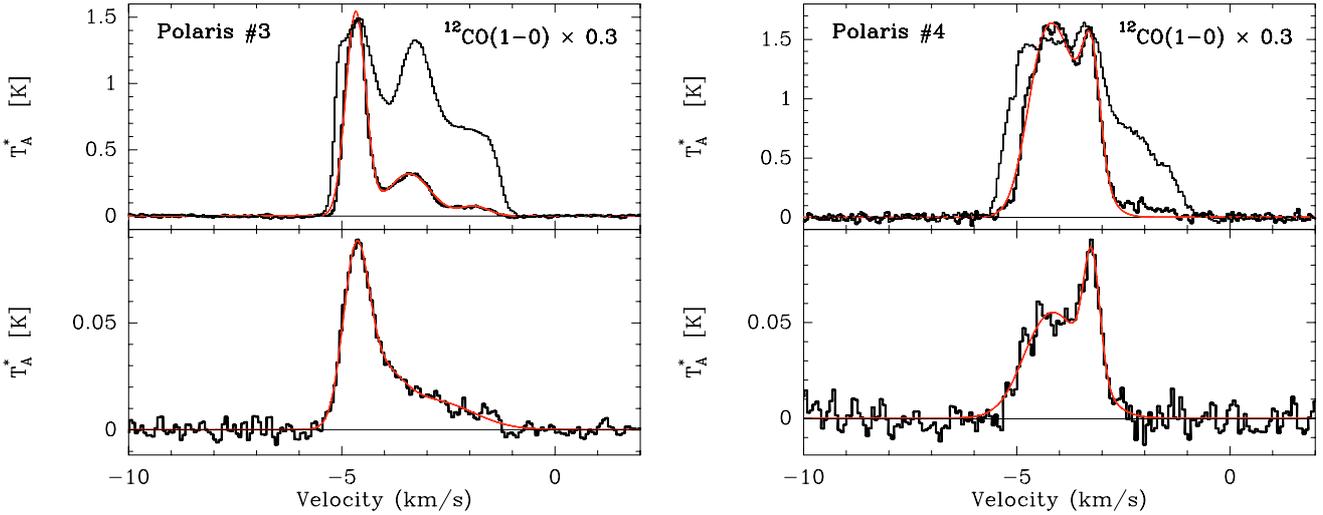
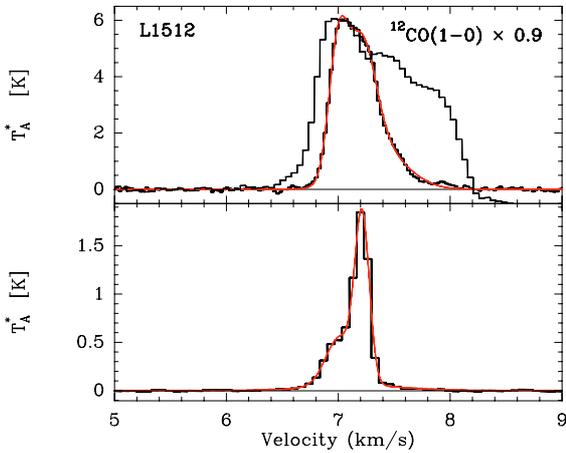**Fig. 4.** Same as Fig. 3 for positions 3 and 4 in Polaris.



**Fig. 5.** Same as Fig. 3 for the position in L1512. Note the very different antenna temperatures, with respect to the Polaris field, for the HCO$^+$ line in particular, due to the fact that the dense core is sampled by the beam in L1512. The velocity scales for the two fields are also very different.
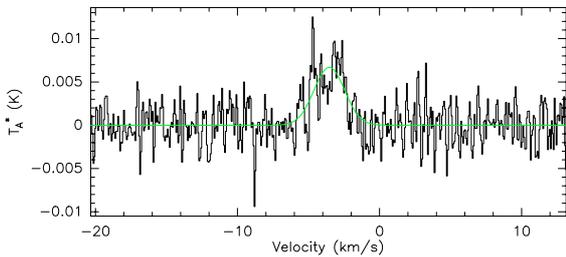


**Fig. 6.** C$_2$H spectrum at position 2 in Polaris. The line parameters derived from the Gaussian fit are: $v = -3.5$ km s$^{-1}$, $T_A^* = 7$ mK, $\sigma = 3$ mK and $\Delta v = 3$ km s$^{-1}$).

and $x_e = 10^{-5}$. The HCO$^+$-electron rates calculated by Faure & Tennyson (2001) were not used, since they only calculate the rates up to $J$=2, while for our calculations higher excitation levels were included. We verified that, at least for higher temperatures, the rates from Faure & Tennyson (2001) and Bhattacharyya et al. (1981) do not differ significantly. Collisional excitation of HCO$^+$ by H$_2$ at high temperature is

implemented by using the cross-sections computed by Flower (2000).

The excitation temperature, optical depth, and emergent intensity in the $J$=1−0 transition of HCO$^+$ were computed for H$_2$ densities ranging between 30 and $10^5$ cm$^{-3}$ and kinetic temperatures $T_k$ = 10 and 250 K. Temperatures as high as 250 K were considered because observations of the $^{12}$CO($J$=3−2) and $J$=4−3 transitions of a few positions in the environment of L1512 reveal larger $^{12}$CO intensities in these transitions than anticipated from the low J lines if the gas is cold and dense. Diluted ($n_{H_2}$ = 200 cm$^{-3}$) and warm ($T_k$ = 250 K) gas is a possible solution (Falgarone et al. 2001). An upper limit $T_k$ = 200 K on the kinetic temperature is provided by the width of the HCO$^+$ velocity components, whose median value is 0.6 km s$^{-1}$. At $T_k$ = 200 K, the thermal velocity of HCO$^+$ is only $v_{th}$ = 0.24 km s$^{-1}$, and the thermal contribution to the linewidth $\Delta v_{th}$ = 0.57 km s$^{-1}$.

Although weak, the HCO$^+$ lines are not optically thin throughout the intensity range 0.01−0.5 K. For densities lower than a few $10^3$ cm$^{-3}$, the optical depth approaches unity, as the excitation temperature drops towards the Cosmic Background temperature. To break the degeneracy of the problem, we used the $^{13}$CO($J$=1−0) and $J$=2−1 lines to constrain the H$_2$ density and temperature domain of the solutions and, as said above, we restricted our analysis to those components of similar kinematic characteristics in the HCO$^+$ and $^{13}$CO spectra. The $^{13}$CO lines are optically thin (or almost thin, in the case of L1512) so that the column density per velocity unit is well determined and the two constraints of the $^{13}$CO($J$=1−0) antenna temperature and $R$(2−1/1−0) line ratio define a narrow track of solutions in the density-temperature plane, which nevertheless spans the whole range from cold/dense to warm/diffuse gas. Each [HCO$^+$, $^{13}$CO] pair of components (i.e. each letter in Col. 5 of Table 1) has then to be interpreted with the set of values ($n_{H_2}$, $T_k$) allowed by the $^{13}$CO lines.

This method provides determinations of the HCO$^+$ column density per unit velocity $N$(HCO$^+$)/$\Delta v$ that do not suffer from the lack of knowledge of the density, a critical parameter for a line that is so difficult to excite. The results for each ($n_{H_2}$, $T_k$) set are displayed in Fig. 8, where the labels on the curves indicate the gas kinetic temperature, given only once on the upper curve. The tracks appear on that figure, from H$_2$ densities in the range $1-2 \times 10^3$ cm$^{-3}$ at temperatures below 15 K and to densities between 100 and 300 cm$^{-3}$ at temperatures above 100 K.

**Table 2.** LVG results for the five template velocity components. $^{13}$**CO(1−0) line:** range of input values for $R(2-1/1-0)$ (Col. 2) and $T_A^*(1-0)$ (Col. 3), result for the $^{13}$CO column density per unit velocity (Col. 4). **HCO⁺(1−0) line:** input $T_A^*$(Col. 5), lower and upper values for the HCO⁺ column density met along the curves shown in Fig. 8 (Col. 6), and corresponding range of $^{13}$CO/HCO⁺ ratios (Col. 7).

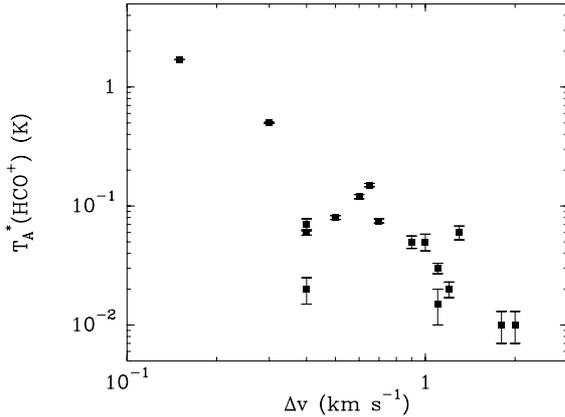| | $R(2-1/1-0)$ | $T_A^*(^{13}\mathrm{CO})$ K | $N(^{13}\mathrm{CO})/\Delta v$ cm$^{-2}$/km s$^{-1}$ | $T_A^*(\mathrm{HCO}^+)$ K | $N(\mathrm{HCO}^+)/\Delta v$ $10^{12}$ cm$^{-2}$/km s$^{-1}$ | $N(^{13}\mathrm{CO})/N(\mathrm{HCO}^+)$ |
|---|---|---|---|---|---|---|
| A | 0.3–0.6 | 0.07–0.2 | $1.2 \times 10^{14}$ | 0.01 | 0.1–0.3 | 1200–400 |
| B | 0.3–0.6 | 0.2–0.5 | $3 \times 10^{14}$ | 0.025 | 0.1–0.25 | 3000–1200 |
| C | 0.3–0.6 | 0.7–1.5 | $1.2 \times 10^{15}$ | 0.09 | 0.7–1 | 1700–1200 |
| D | 0.5–0.6 | 2.–3. | $2. \times 10^{15}$ | 0.24 | 1.2–2.3 | 1667–870 |
| E | 0.55–0.65 | 5.–7. | $7.2 \times 10^{15}$ | 0.5 | 2.5–4.0 | 2880–1800 |



**Fig. 7.** Peak antenna temperature versus half-power linewidth of all the Gaussian components identified in the HCO⁺(1−0) line profiles and listed in Table 1.
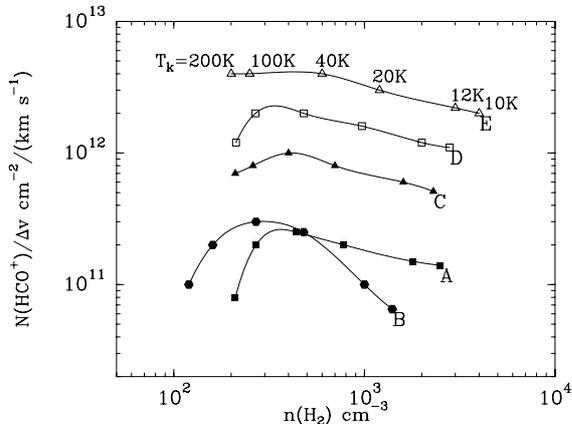


**Fig. 8.** HCO⁺ column densities per unit velocity as a function of H$_2$ density, for the five template components (A to E) for which the LVG analysis is possible (see text). Six values of the kinetic temperature are given along the upper curve, the same values being marked by the 6 symbols on the other curves. Each $(n_{\mathrm{H}_2}, T_k)$ set belongs to the narrow track of solutions allowed by the CO data (Sect. 3).

In the following discussion, we restrict the domain of $T_k$ to a range 15−20 K to 200 K, the lower value being the temperature of a gas of density $1-2 \times 10^3$ cm$^{-3}$, shielded from the solar neighborhood UV field by 0.5 to 1 mag (Le Petit et al. 2004), the upper limit corresponding to a fully thermal contribution to HCO⁺ line widths of 0.57 km s$^{-1}$.

In spite of the large range of kinetic temperatures considered, $20 < T_k < 200$ K, Fig. 8 shows that the HCO⁺ column density of each component is determined to within a factor of a few (see

also Table 2). Their values for the ensemble of the five template components span more than one order of magnitude.

The main difficulty in the derivation of the HCO⁺ abundances from the above set of column densities, is the estimate of the relevant hydrogen column density of each component. This is so because each component is defined only by its velocity and velocity width and contributes to only a small fraction of the total column density. In the following expression of the HCO⁺ abundance:

$$X(\mathrm{HCO}^+) = \left(\frac{N(\mathrm{HCO}^+)}{\Delta v}\right) \Delta v \frac{1}{n_{\mathrm{H}} L}, \tag{1}$$

$\frac{N(\mathrm{HCO}^+)}{\Delta v}$ and $n_{\mathrm{H}}$ are derived from the above LVG analysis for each case, and $\Delta v$ is known from the data. Here, $n_{\mathrm{H}} = 2n_{\mathrm{H}_2}$ is the density of protons in a gas where the density of atomic hydrogen has been neglected, according to PDR models for gas with UV shieldings above 0.2 mag (Le Petit et al. 2004). The depth $L$ is the only independent, unknown and free parameter in the derivation of $X(\mathrm{HCO}^+)$. An estimate of the depth $L$ is thus needed for each velocity component. The channel maps in the $^{12}$CO($J=2-1$) lines (Figs. 1 and 2) have been used to estimate the spatial extent in projection, $L$, of each of the velocity components. The similarity of the velocity coverages of the $^{12}$CO and HCO⁺ lines suggests that at the scale of the resolution these species are well mixed in space too. The lengthscale $L$ characteristic of the structures are all on the order of 0.05 pc in projection. The actual lengthscale over which the line forms may be longer by a factor of a few, less than 10 on statistical grounds (then the filaments would be the edge-on projection of sheets) or smaller if substructure exists. In the following, we adopt $L = 0.1$ pc for all the components. Note that the estimated total column density of individual velocity components thus ranges from $N_{\mathrm{H}} = 7.5 \times 10^{19}$ cm$^{-2}$ to ten times more, or $0.04 < A_{\mathrm{V}} < 0.4$, which is smaller, as expected, than the cloud visual opacities discussed in Sects. 2 and 4.2. A velocity coverage $\Delta v = 0.5$ km s$^{-1}$ has been adopted for all the components as the median value of the well-identified components in Table 1. The broadest components are probable collections of narrower sub-components. The results are shown in Fig. 9 for the five cases analyzed. The symbols are the same as in Fig. 8, and on each curve they mark the set of kinetic temperatures, $T_k = 20$, 40, 100 and 200 K from right to left. According to the previous discussion, these abundances may have been over or underestimated by a factor 3 at most. We compare these determinations to results of chemical models in Sect. 4.

### 3.2. C₂H

The width of the C$_2$H line is large and probably corresponds to the weakest component seen in the HCO⁺ profile at the same
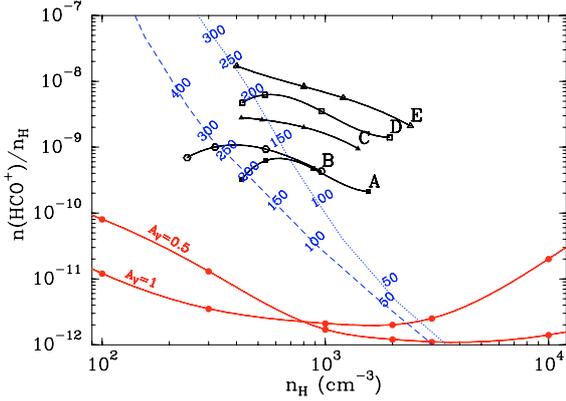
**Fig. 9.** HCO$^+$ abundances as a function of the hydrogen nuclei density. The five upper curves (thick solid curves) are the tracks derived from the observations displayed with the same symbols as in Fig. 8. The kinetic temperature varies along each curve and the symbols are located at $T_k$ = 20, 40, 100 and 200 K from right to left. The ($n_H$, $T_k$) sets are those inferred from the CO data. Thick lower curves (red): results of steady-state chemistry models, computed for two different values of the UV shielding, $A_v$ = 0.5 and 1 mag. Dashed and dotted curves (blue): tracks of non-equilibrium chemical computations along two isobaric cooling sequences (see Sect. 4.4). The initial conditions are the same ($n_H$ = 100 cm$^{-3}$) except for the shielding from the ISRF: $A_V$ = 0.2 mag (dashed) and $A_V$ = 1 mag (dotted). On each of them, the gas temperature decreases from top to bottom and is given along each track to allow a comparison of the LVG and chemical solutions in the $[X(\text{HCO}^+), n_H, T_k]$ space.

position (case A). With only one transition detected, one can simply estimate the column density by assuming the excitation temperature and low opacity. For $A_{3/2,2-1/2,1}$ = 4.1 × 10$^{-7}$ s$^{-1}$ and an excitation temperature of 10 K, the inferred column density is $N(\text{C}_2\text{H})$ = 2 × 10$^{12}$ cm$^{-2}$. The corresponding abundance, is $X(\text{C}_2\text{H})$ = 2 × 10$^{-8}$ for an estimated total column density $N_H \approx 10^{20}$ cm$^{-2}$ from $n_H \approx 500$ cm$^{-3}$ (Fig. 9) and $L$ = 0.1 pc.

At this position, the same component has $N(\text{HCO}^+)$ = 3 × 10$^{11}$ cm$^{-2}$, which makes this component similar to the weakest lines detected by Lucas & Liszt (2000) in diffuse molecular clouds, with an abundance ratio C$_2$H/HCO$^+ \approx$ 7, consistent with the non-linear relationship they find between these two species.

# 4. Comparison with chemical models

## 4.1. Description of the steady-state model for chemistry

Steady-state HCO$^+$ abundances were computed using the Meudon PDR code[2]. Models here consider semi-infinite clouds of constant density in plane-parallel geometry with ionizing photons coming from one side. The UV spectral density of the photons is scaled according to the Draine radiation field (Draine 1978). The dust extinction curve is the galactic one as parameterized by Fitzpatrick & Massa (1990). The computation proceeds from the exterior and penetrates into the cloud. At each step, chemical and thermal equilibrium are reached self-consistently. Radiative cooling makes use of the on-the-spot approximation that considers that an emitted photon is either re-absorbed locally or escapes from the cloud, and line emissivities depend on the abundances. Radiative transfer into lines of H$_2$ and CO is computed using the approximation of Federman et al. (1979). The depth into the cloud is measured in magnitudes of visual

---

[2] Code available at
http://aristote.obspm.fr/MIS/index.html

extinction ($A_V$). Therefore, $A_V$ = 0 mag at the edge of the illuminated cloud, increasing when moving deeper into it. One is then free to consider some particular points in the cloud, corresponding to particular visual extinctions.

We computed the abundance of HCO$^+$ in several models with different hydrogen densities, and plot the result at two depths in the cloud, $A_V$ = 0.5 and 1 mag (see Fig. 9). Since the total extinction in the direction of the observed positions is smaller than 1 mag (see Sect. 2.1), except for the gas in the L1512 dense core not under consideration here, it is reasonable to assume that *locally* the UV shielding is also less than 1 mag, hence the two PDR cases shown in Fig. 9.

## 4.2. Lack of steady-state chemical solutions

Figure 9 shows that none of the HCO$^+$ abundances derived from the observations are consistent with steady-state chemistry in clouds moderately shielded from the ambient UV field, even at high density. The uncertainties in the abundance derivations are large and due mostly to the unknown extent of the emitting gas along the line of sight $L$. Note, however, that a depth 10 to 100 times larger (i.e. 1 to 10 pc) would be required to bring the curves deduced from the observations down to the domain of steady-state solutions. Depths larger than ~3 pc are ruled out by the average column density in the fields, $A_V < 1$. Structures smaller than 0.1 pc are indeed suggested by the PdBI observations reported in Paper III. We thus conclude that the observed HCO$^+$ abundances cannot be produced by state-of-the-art models of gas phase steady-state chemistry in diffuse molecular clouds.

## 4.3. Non-equilibrium chemistry

An alternative scenario relies on the proposal that small regions bearing different chemical signatures from those of the bulk of gas are permanently generated in interstellar matter by bursts of turbulence dissipation. The space-time intermittency of turbulence dissipation is such that the heating rate due to the local release of suprathermal energy may exceed those driven by the UV radiation field. In low density gas and in the UV field of the Solar Neighborhood, this is the case as soon as dissipation is concentrated in less than a few % of the volume (see the review of Falgarone 1999).

Intermittent dissipation locally heats the gas far above its average equilibrium temperature, over a timescale that is sufficient to trigger a specific chemical network driven by endothermic reactions or involving large activation barriers. In the regions heated by the non-thermal energy from turbulence, the endothermic barrier ($\Delta E/k$ = 4640 K) of the C$^+$ + H$_2 \rightarrow$ CH$^+$ + H reaction is overcome, and it occurs at a much higher rate than the slow radiative associations, C$^+$ + H $\rightarrow$ CH$^+$ + $h\nu$ and C$^+$ + H$_2 \rightarrow$ CH$_2^+$ + $h\nu$ (Black et al. 1978). Such a scenario was first suggested by the good correlation observed between CH$^+$ column densities and rotationally excited H$_2$ (Lambert & Danks 1986). The CH$^+$ ions then initiate the hydrogenation chain, CH$^+$ + H$_2 \rightarrow$ CH$_2^+$ + H and CH$_2^+$ + H$_2 \rightarrow$ CH$_3^+$ + H, which does not proceed further because CH$_3^+$ recombines with electrons faster than it reacts with H$_2$. In the regions heated by non-thermal bursts of energy, CH$_3^+$ thus becomes the most abundant ion. As discussed in the specific model of JFPF, it is even more abundant than CH$^+$ because its formation rate stays higher than its destruction rate. It opens up a new route for the formation of HCO$^+$,

$$\text{CH}_3^+ + \text{O} \rightarrow \text{HCO}^+ + \text{H}_2. \tag{2}$$

Large amounts of HCO$^+$ are thus expected to be produced by this chemistry, even in regions that are weakly shielded from the UV field. There, HCO$^+$ is, in part, a daughter molecule of CH$^+$, although other routes are also active (see Sect. 5).

Following Moffatt et al. (1994), the regions of intermittent dissipation have been modeled in JFPF by Burgers vortices threaded by helical magnetic fields, an alternative scenario to magneto-hydrodynamic (MHD) shocks in the absence of an obvious post-shock compressed layer. The vortex is fed by large scale motions. Its lifetime is therefore the turnover time of these large scales, on the order of ten times (or more) its own period, $P$. Therefore, the characteristics of the vortex are not free parameters but imposed by the ambient turbulence. Viscous dissipation is concentrated in the layers of large velocity shear at the edge of the vortex. In magnetized vortices of the cold neutral medium (CNM), JFPF show that decoupling occurs between the neutrals spiralling in and the ions tightly coupled to steady helical fields. An additional local heating rate, due to the friction between the ions and the neutrals, is thus present. The chemistry in the diffuse gas reacts swiftly to the sharp increase in gas temperature generated by turbulence dissipation. In the model of JFPF, relevant for the CNM, the period of the vortex is $P = 600$ yr, its lifetime $\approx 10^4$ yr, and the minimum time to build up the molecular abundances specific to the warm chemistry is $t_{\rm warm} \approx 200$ yr.

The sequence of events we consider is therefore: diffuse gas enters such a vortex (or an ensemble of vortices braided together), spiralling inward. It is heated and enriched chemically during at least 200 yr while it crosses the layers of largest velocity shear and largest ion-neutral drift, the *active* layers of the vortex. Then it enters the central regions of the vortex where the temperature drops due to the decrease in dissipation. The gas formerly heated and chemically enriched starts cooling down and condensing self-consistently with its chemistry. Its radial velocity there has become vanishingly small. Eventually, the vortex blows-up after $\approx 10^4$ yr.

The thermal and chemical evolution of the gas in the *active* warm layers of the vortex was computed in JFPF. In the present work, we follow the time-dependent evolution of the density, temperature and chemical abundances of the gas, once it has left these active layers. An isobaric evolution is assumed. We used another code with the same chemical network and the same cooling functions. The time-dependent evolution was computed for a given and constant shielding from the UV field. The gas temperature was derived from the radiative cooling rate that depends on the chemical abundances, the H$_2$ density and temperature.

The results are displayed in Fig. 10 for four different initial conditions in density and shielding from the UV field. Two initial densities are considered, $n_{\rm H} = 30$ and $100$ cm$^{-3}$, representative of the CNM. The *local* heating rate due to turbulent dissipation, $\Gamma_{\rm d}$, characterizes the strength of the burst. Two values are chosen, $\Gamma_{\rm d} = 10^{-21}$ erg cm$^{-3}$ s$^{-1}$ for the densest case and $\Gamma_{\rm d} = 10^{-23}$ erg cm$^{-3}$ s$^{-1}$ for the other, so that the initial kinetic temperature is close to $10^3$ K in each case. These values correspond to the *average* heating rate due to turbulence dissipation in the CNM, $\overline{\Gamma}_{\rm d} = 2 \times 10^{-25}(\overline{n}_{\rm H}/30 \, {\rm cm}^{-3})$ erg cm$^{-3}$ s$^{-1}$, divided by the estimated volume-filling factor of the gas affected by the burst, or $\approx 2 \times 10^{-2}$ for the weaker type of burst and $\approx 10^{-3}$ for the stronger and therefore rarer type (see the discussion in JFPF and Falgarone 1999). Two values of the shielding from the ambient ISRF are also considered, $A_{\rm V} = 0.2$ and 1 mag to bracket the conditions prevailing in the gas under study. The ionization degree stays close to $x_{\rm e} = 10^{-4}$ along the isobaric evolution at $A_{\rm V} = 0.2$ and varies between $x_{\rm e} = 10^{-4}$ and $10^{-5}$ in the other case, following the chemical evolution of the ions. These upper
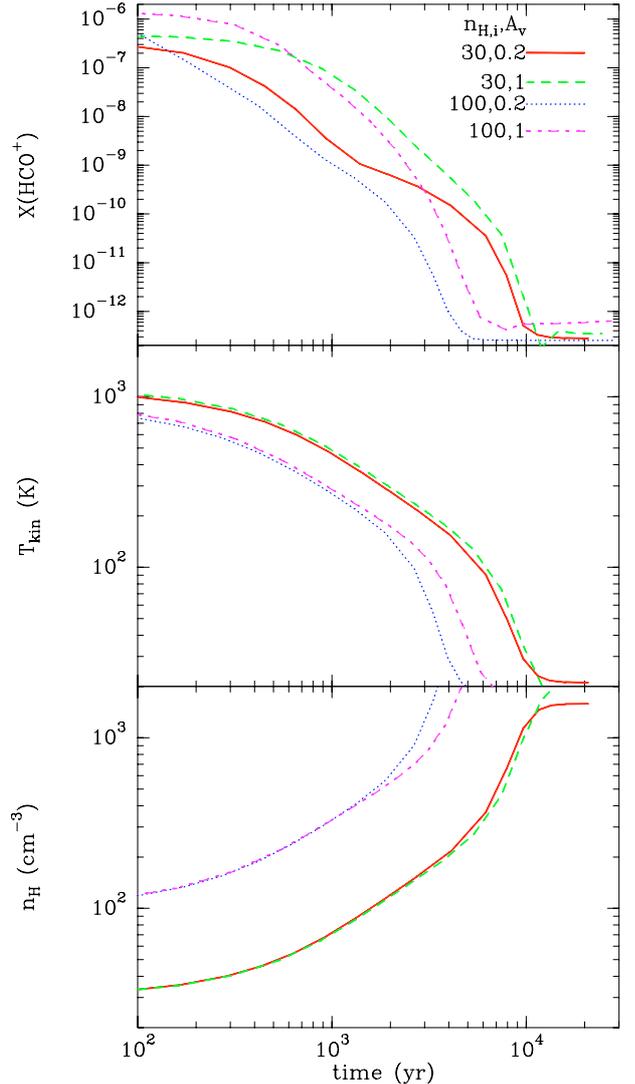


**Fig. 10.** Time-dependent evolution of (*top*) the HCO$^+$ abundance, (*middle*) the kinetic temperature, and (*bottom*) the hydrogen density, along the isobaric cooling of a parcel of gas formerly enriched chemically in a burst of dissipation of turbulent energy. The initial densities are $n_{\rm H,i} = 30$ (dashed and solid) and 100 cm$^{-3}$ (dotted and dot-dashed), and the shieldings from ISRF are $A_{\rm V} = 0.2$ (solid and dotted) and 1 mag (dashed and dot-dashed).

and lower values of $x_{\rm e}$ are those used in the LVG code. The initial chemical abundances are those produced by the warm chemistry in the active layers of the vortex, as computed by JFPF.

It is remarkable that the signatures of the warm chemistry are kept by the gas for more than $10^3$ years after the gas has escaped the active layers. The curves of Fig. 10 illustrate the marked non-linearity of the chemical evolution: (1) large differences are visible after only $10^3$ years between the tracks followed by two parcels of gas with very similar initial conditions; (2) $X$(HCO$^+$) drops by 6 orders of magnitude, while the density and temperature vary by a factor 50 only.

### 4.4. Existence of [$X$(HCO$^+$),$n_{\rm H}$, $T_{\rm k}$] tracks crossing the observation domain

We show below that we may have detected the decaying signatures of the warm chemistry generated by bursts of turbulence dissipation. The time-dependent evolution of an enriched

**Table 3.** Sets of non-equilibrium HCO⁺ abundances consistent with HCO⁺(J=1−0) line observations. Each solution is given as a range of values for the set $[X(HCO^+), n_H, T_k]$ corresponding to the range of observed values (cases A to E). The parameters of the models are the turbulent heating rate $\Gamma_d$, the shielding from the UV field $A_v$, and the initial density $n_{H,i}$.

| $\Gamma_d$ erg cm$^{-3}$ s$^{-1}$ | $A_v$ | $n_{H,i}$ cm$^{-3}$ | $X(HCO^+)$ | $n_H$ cm$^{-3}$ | $T_k$ K |
|---|---|---|---|---|---|
| $10^{-21}$ | 0.2 | 100 | $8-2 \times 10^{-10}$ | 320–500 | 250–150 |
| $10^{-21}$ | 1 | 30 | $3-0.5 \times 10^{-9}$ | 130–200 | 250–170 |
| $10^{-21}$ | 1 | 100 | $6-1.6 \times 10^{-10}$ | 700–900 | 150–120 |
| $10^{-23}$ | 0.2 | 30 | $9-3 \times 10^{-9}$ | 80–130 | 250–160 |
| $10^{-23}$ | 1 | 100 | $7-1 \times 10^{-9}$ | 100–120 | 250–220 |

parcel of gas, once the heating due to dissipation of turbulence has dropped, is a curve in the $[X(HCO^+), n_H, T_k]$ space that depends on the initial conditions and on UV shielding (see Fig. 10). It is therefore not straightforward to compare it with observational results. As an illustration that such an evolution is consistent with our data, we have drawn two of the tracks of Fig. 10 (those corresponding to the largest initial density) in the $[X(HCO^+)−n_H]$ plane of Fig. 9. On each of them, the gas temperature decreases from top to bottom from about 500 to 50 K. In that plane, the LVG solutions and the cooling tracks are almost perpendicular. The only temperature range where they are consistent is the range 100−300 K: the low-extinction track is consistent with the LVG solutions for components A and B and the more shielded evolution for all the others (C, D and E).

The range of values of the HCO⁺ abundances, density and kinetic temperature of the part of the isobaric cooling consistent with the observations (cases A to E) is given in Table 3 for five different sets of initial conditions, including the strength of the dissipation burst that determines the local heating rate, $\Gamma_d$.

We have not explored a larger domain of initial conditions because our goal here is only to illustrate the compatibility of such a non-equilibrium chemistry with the data. A more detailed analysis requires further constraints to treat the many non-linearities of the physics and chemistry involved and explore a relevant part of the vast parameter space. Moreover, our model, although complex in terms of coupled processes, is still too crude. For instance, we have neglected the initial dynamical expansion of the warm gas because the radiative cooling and chemical timescales, up to ∼a few thousand years, are smaller than the expansion time of the warm gas under the effect of pressure gradient, just after the burst of dissipation. The timescale for a warm structure of initial thickness $L_0$ to double its size under expansion at the sound velocity in the ambient cold neutral medium ($c_S \sim 0.5$ km s$^{-1}$) is $2 \times 10^5 (L_0/0.1$ pc) yr. Were they much smaller, the timescale would be shorter. The Lorentz force acting on the ions somewhat delays the expansion at a rate that depends on the gas ionization degree and geometry of the helical magnetic fields.

Nonetheless, the above comparison brings to light a few interesting results: all the solutions provided by the non-equilibrium chemistry consistent with the observations are warmer than 100 K (Table 3) and the inferred HCO⁺ abundances are all larger than $2 \times 10^{-10}$ and as large as $\approx 10^{-8}$. They are more than one order of magnitude above the values computed at steady-state at densities less than $10^3$ cm$^{-3}$. It is remarkable that these abundances bracket the value $X(HCO^+) = 2 \times 10^{-9}$ determined by Lucas & Liszt (1996) and Liszt & Lucas (2000) from their observations of the HCO⁺(J=1−0) line in absorption

against extragalactic continuum sources. These lines of sight sample the ordinary interstellar medium of low visual extinction (many of the extragalactic background sources are visible QSOs) as opposed to dense cores and star-forming regions. It is thus plausible that their observations sample the kind of molecular material we discuss here, their inferred abundances being an average along the lines of sight of HCO⁺-poor and HCO⁺-rich regions. Finally, these results are weakly sensitive to the strength of the dissipation burst, as if the actual initial conditions were rapidly forgotten.

### 4.5. The HCO⁺ enrichment and the strength of the velocity shear

As seen in Table 1, the five observed positions do not sample gas with similar kinematic properties: two positions (Polaris #2 and 3) lie on the locus of largest velocity shears in the Polaris field (i.e. populating the non-Gaussian tails of the probability distributions of CVIs, Pety & Falgarone 2003). The others correspond to smaller velocity shears. Against all expectations (Table 1), the largest HCO⁺ abundances (D, E, and dc components) are found at those positions of smallest CVIs, while the set of least chemically enriched components (A, B, and C) are found at the positions with the largest CVIs. Since the dissipation rate and therefore the gas temperature increases with the strength of the velocity shear, one expects that the chemical enrichment would increase with the velocity shear or the CVIs. It is not what is observed.

These results suggest a broader time sequence, encompassing the relaxation scheme discussed in the previous section, in which the increase of HCO⁺ abundance is a measure of the elapsed dissipation: the longer the dissipation has been going on, the smaller the velocity shear (i.e. the vortex has started to fade), and the larger the quantity of chemically enriched gas produced. Such a sequence is also suggested by the rough anticorrelation displayed in Fig. 7. The HCO⁺ column density of each component being close to $T^*_{A_i} \Delta v_i$ since the line is not very optically thick, it increases as the velocity dispersion decreases, as $\Delta v_i^{-1}$. The observed quantity of chemically enriched gas is produced at the expense of the non-thermal kinetic energy traced by $\Delta v_i$.

## 5. Discussion and perspectives

### 5.1. The complex space-time average hidden in the observed HCO⁺ emission lines

The results of the last section seem to contradict the relaxation scenario described above, in which the HCO⁺ abundance decreases with time. Another, probably related question, is why, in view of the six orders of magnitude spanned by the HCO⁺ abundance in the proposed non-equilibrium evolution, the observations in emission point to a much narrower range of abundances, $2 \times 10^{-10} < X(HCO^+) < 10^{-8}$. This may be understood within a framework in which several phases of the evolution are present simultaneously in the beam. This is possible because individual vortices in the JFPF model are much thinner than the IRAM-30 m beamsize of 0.015 pc or ≈3000 AU. Observations sample a mixture of gases located at decreasing distances from the vortex axis: (i) the most diluted and HCO⁺-rich gas, still in the warm active layers of the vortices, as long as they are alive; (ii) gas already out of the warm active layers and relaxing; and (iii) the densest, coldest and HCO⁺-poor gas. The older the burst, the larger the amount of relaxed gas. The signal detected in emission is sensitive to a combination of (i) the HCO⁺ column

density or simply the abundance $X(t)$ (assuming the total gas column density being processed is constant with time); (ii) the density $n_H(t)$ that enters the line excitation and (iii) a term involving the duration of the phase, $\approx t$, given the broad range of timescales involved. We computed the time integral of $X(t) n_H(t)$, taken as a template for the signal in emission, assuming that we observe all the phases in the gas accumulated during at least $\approx 10^4$ yr, the lifetime of the vortex. For all the cases, this quantity increases linearly with time up to a maximum at about $10^3$ yr and does not increase further. The observations in emission are thus likely to be most sensitive to the the relaxation phase because it lasts longer and involves denser gas than the brief phase of chemical enrichment in gas that is too diluted to significantly excite the HCO$^+$(1−0) line.

In contrast, the intensity of the HCO$^+$ absorption line is not sensitive to the gas density. The warmest and richest phase of the evolution may have been detected by Liszt & Lucas (2000) as the broad and weak absorption seen in the direction of B0355+508 over the whole velocity extent of the H I absorption line.

More detailed comparison between abundances inferred from observations in absorption and in emission involves time and space averages that cannot be achieved at this stage of the study. The present observations were obtained on one single ensemble of such dissipative structures, possibly generated simultaneously. Thus, space/time average is probably simpler than that required to interpret absorption measurements that sample depths of gas on parsec scales.

### 5.2. More support for non-equilibrium chemistry: "warm"-molecule abundance ratios

The present work stresses the need for a non-equilibrium mechanism to explain the large abundances of HCO$^+$ detected in gas of moderate density and poorly shielded from the ambient ISRF. In this scenario, the gas is driven locally past a high-temperature threshold by an impulsive release of turbulent energy. Once the gas has escaped the region of large dissipation, it cools down and condenses, and the chemistry evolves accordingly.

Our results are independent of any details of the processes at the origin of the warm chemistry. Flower & Pineau des Forêts (1998) and Gredel et al. (2002) have shown that slow MHD shocks of velocities $V_s \sim 10$ km s$^{-1}$ reproduce the OH/HCO$^+$ abundance ratios observed in the diffuse medium (Lucas & Liszt 1996). In MHD shocks, as in magnetized coherent vortices, gas is temporarily heated to temperatures as high as $10^3$ K. The triggered warm chemistry is characterized by coexisting large abundances of OH, H$_2$O, HCO$^+$, and CH$^+$, water and HCO$^+$ being daughters of OH and CH$^+$, respectively (JFPF). Their time-dependent evolution in the relaxation phase is displayed in Fig. 11 for one of the cases discussed in Sect. 4 (initial density $n_{H,i} = 100$ cm$^{-3}$, $\Gamma_d = 10^{-21}$ erg cm$^{-3}$ s$^{-1}$, and $A_V = 1$). The abundance ratios along this evolution are interesting in their marked differences (Fig. 12). The H$_2$O/OH ratio varies by less than a factor 3 along the time-dependent evolution, up to $10^3$ yr after the beginning of the relaxation, and stays close to the values found in diffuse molecular clouds by the *SWAS* satellite (Neufeld et al. 2002; Plume et al. 2004). The OH/HCO$^+$ ratio varies by more than a factor 10 along the same evolution. We note, however, that its variations bracket the average value OH/HCO$^+ \sim 30$ found by Lucas & Liszt (1996) in their random sampling of the diffuse ISM provided by their absorption lines survey towards extragalactic sources. In contrast, the CH$^+$/HCO$^+$ ratio varies very little, only before $10^3$ yr. The value of the ratio, though, critically depends on the density (JFPF). This follows from the
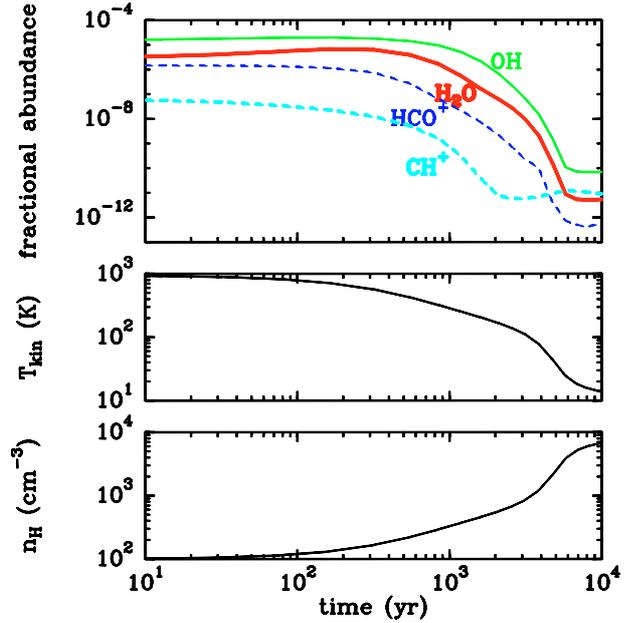


**Fig. 11.** Time-dependent evolution of *(top)* the OH (thin solid), H$_2$O (thick solid), HCO$^+$ (dashed), and CH$^+$ (thin dashed) abundances, *(middle)* the kinetic temperature and *(bottom)* the total hydrogen density, along the isobaric cooling of a parcel of gas formerly enriched chemically in a burst of dissipation of turbulent energy. The initial conditions here are $n_{H,i} = 100$ cm$^{-3}$, $\Gamma_d = 10^{-21}$ erg cm$^{-3}$ s$^{-1}$, and the shielding from ISRF $A_V = 1$.
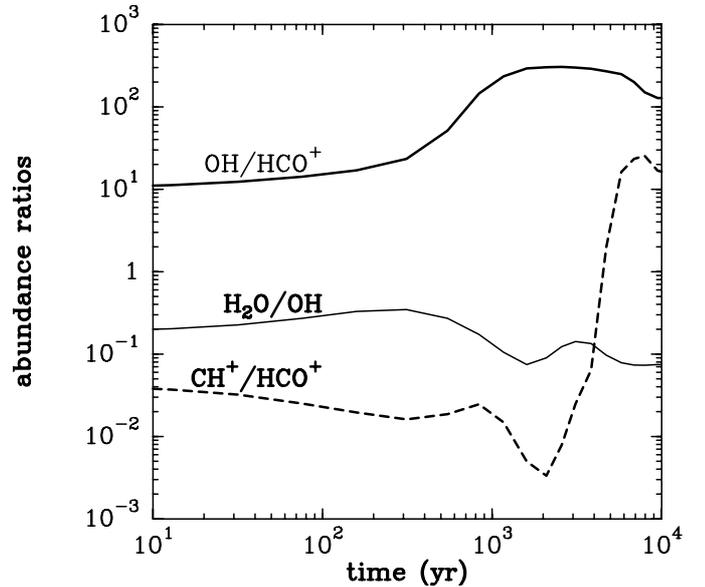


**Fig. 12.** Time-dependent evolution of abundance ratios, OH/HCO$^+$ (thick), H$_2$O/OH (thin), and CH$^+$/HCO$^+$ (thick dashed), along the same isobaric cooling as in Fig. 11.

fact that in our model of warm chemistry, HCO$^+$ is not only a daughter molecule of CH$^+$. It also forms via other routes such as CO$^+$ + H$_2$ → HCO$^+$ + H, triggered by the endothermic charge exchange between H$^+$ and O ($\Delta E/k = 227$ K), and H$_3^+$ + CO → HCO$^+$ + H$_2$, also slightly enhanced in warm chemistry because both CO and H$_3^+$ have increased abundances in the warm layer of the vortex. This route may even be a dominant formation scheme for HCO$^+$, if the large abundance of H$_3^+$ detected on the line of

sight towards $\zeta$ Per by McCall et al. (2003) happens to be the rule in the diffuse ISM.

There is also an efficient channel to form $C_2H$ in the warm chemistry. It proceeds via the endothermic reaction ($\Delta E/k = 1760$ K) CH + H$_2\rightarrow$ CH$_2$ + H, followed by a series of fast reactions: C$^+$ + CH$_2$ $\rightarrow$ C$_2$H$^+$ + H, the hydrogenation of C$_2$H$^+$ into C$_2$H$_2^+$, the recombination of C$_2$H$_2^+$, and terminating with photodissociation of C$_2$H$_2$, which provides C$_2$H.

These results are encouraging and suggest that impulsive chemical enrichment of the CNM by turbulence dissipation bears observable signatures up to several 10$^3$ yr after the end of the enrichment.

### 5.3. Large scale signatures of small scale activity

Other signatures, independent of chemistry, have been found for the existence in the CNM of gas at a few hundred Kelvin. They comprise collisional excitation of H$_2$ far from UV sources susceptible to generate fluorescence (Gry et al. 2002; Lacour et al. 2005; Falgarone et al. 2005). In the first two cases, H$_2$ is detected in UV absorption against nearby late B stars, while in the third case, the pure rotational lines of H$_2$ have been observed along a long line of sight across the Galaxy avoiding star-forming regions. The rotational temperature of the warm H$_2$ in these data is 276 K. In all cases the fraction of warm H$_2$ in the total column of gas sampled is the same, on the order of a few percent. It is the same fraction as that required in the Solar Neighborhood to reproduce the large observed abundances of CH$^+$ within the CNM (JFPF). A few percent of warm gas, for which UV photons cannot be the sole heating source, is ubiquitous in the cold diffuse medium.

Finally, we would like to stress the spatial scales presumably involved in the framework of the existing model, where individual vortices have transverse column densities as small as $N_H \approx 2\times10^{16}$ cm$^{-2}$ corresponding to initial values of $n_{H,i} = 100$ cm$^{-3}$ and $l_i = 15$ AU (JFPF). We illustrate the point with the case C solutions: $N(HCO^+) \approx 8 \times 10^{11}$ cm$^{-2}$, $X(HCO^+) \approx 2 \times 10^{-9}$, $n_H \approx 500$ cm$^{-3}$. The total column density of observed material is thus $N_H = N(HCO^+)/X(HCO^+) = 4\times10^{20}$ cm$^{-2}$, corresponding to $2 \times 10^4$ vortices in the IRAM beam. Here we assume that the isobaric evolution occurs at constant mass, so that the transverse column density of vortices remains the same. For the gas at 500 cm$^{-3}$, the transverse size has a thickness of about 3 AU. The ensemble of the $2 \times 10^4$ vortices, probably braided together, as vortex tubes do (e.g., Porter et al. 1994), would form an elongated structure about 450 AU thick, if the vortices are in contact with one another. The IRAM beam at the distance of the sources is a few times larger, and the size of the structure seen with the PdBI is of this order of magnitude (Paper III). This rough estimate just shows that the existence of chemical inhomogeneities on AU scales is not ruled out in the diffuse ISM. It would certainly help for understanding the remarkable similarity of the OH and HCO$^+$ absorption line profiles reported by Liszt & Lucas (2000).

Chemical and thermal relaxation timescales are so short compared to the dynamical lifetime of molecular clouds (of at least a million year) that all the stages of the above evolution should co-exist along a random line of sight. At present, the receiver sensitivity and the telescope beam sizes provide, when observed in emission, a signal that is the space and time average of myriads of small unresolved structures, most likely caught at different epochs in their evolution. Molecular line observations in absorption in the UV, visible, and now submm domains

are much more sensitive and have presumably already started to sample this apparently untractable complexity.

## 6. Summary

This work is part of a broad study dedicated to those singular regions in the environment of low-mass dense cores, characterized by non-Gaussian velocity shears in the statistics of the turbulent velocity field of the clouds. These regions have been proposed as the sites of intermittent dissipation of turbulence in molecular clouds, and the large *local* release of non-thermal energy in the gas there has been shown to be able to trigger a specific warm chemistry, in particular to explain the large abundances of CH$^+$, H$_2$O, and HCO$^+$ observed in diffuse gas.

We report here the first detection of HCO$^+$(1−0) line emission in two of these singular regions. The HCO$^+$ abundances inferred from the data cannot be explained by steady-state chemistry driven by UV photons because the gas temperature is too low and the HCO$^+$ abundances formed are too small by more than an order of magnitude. As a follow-up to the model proposed by JFPF, we have computed the time-dependent evolution of the specific chemical signatures imprinted in the gas by the short bursts of turbulence dissipation (a few 100 years), once the gas has escaped the layers of active warm chemistry. We show that the signature of the warm chemistry survives in the gas for more than 10$^3$ yr and that the density (a few 100 cm$^{-3}$), the temperature (a few hundred Kelvin), and the large HCO$^+$ abundances ($2 \times 10^{-10}$ to $10^{-8}$) inferred from the observations can be understood in the framework of this thermal and chemical relaxation, while steady-state chemistry driven by UV photons fails by more than one order of magnitude.

The large abundances detected in the present work, and probably the many signatures of a warm chemistry now found in diffuse gas, are thus probably due to the slow chemical and thermal relaxation of the gas following the large impulsive releases of energy on small scale due to intermittent dissipation of turbulence. The detailed confrontation of our model with available data relevant to the existence of a warm chemistry going on in cold, diffuse gas involves complex time and space averaging, but abundance ratios among H$_2$O, OH, HCO$^+$, and CH$^+$ already suggest that such non-equilibrium processes on AU scale are at work in diffuse clouds.

## References

Abergel, A., Boulanger, F., Mizuno, A., & Fukui, Y. 1994, ApJ, 423, L59
Bhattacharyya, S. S., Bhattacharyya, B., & Narayan, M. V. 1981, ApJ, 247, 936
Black, J. H., Hartquist, T. W., & Dalgarno, A. 1978, ApJ, 224, 448
Cambrésy, L., Boulanger, F., Lagache, G., & Stepnik, B. 2001, A&A, 375, 999
Crane, P., Lambert, D. L., & Scheffer, Y. 1995, ApJS, 99, 107
Draine, B. T. 1978, ApJS, 36, 595
Falgarone, E., & Phillips, T. G. 1996, ApJ, 472, 191
Falgarone, E., Phillips, T. G., & Walker, C. 1991, ApJ, 378, 186
Falgarone, E., Panis, J.-F., Heithausen, A., et al. 1998, A&A, 331, 669
Falgarone, E. 1999, in Interstellar Turbulence, ed. J. Franco, & A. Carramiñana (Cambridge Univ. Press)
Falgarone, E., Pety, J., & Phillips, T. G. 2001, ApJ, 555, 178
Falgarone, E., Verstraete, L., Pineau des Forêts, G., & Hily-Blant, P. 2005, A&A, 433, 997
Falgarone, E., Pety, J., & Hily-Blant, P. 2006, in prep. (Paper III)
Faure, A., & Tennyson, J. 2001, MNRAS, 325, 443
Federman, S. R., Glassgold, A. E., & Kwan, J. 1979, ApJ, 227, 466

Fitzpatrick, E. L., & Massa, D. 1990, ApJS, 72, 163

Flower, D. R. 2000, MNRAS, 313, L19

Flower, D., & Pineau des Forêts, G. 1998, MNRAS, 297, 1182

Fuller, G. A., & Myers, P. C. 1993, ApJ, 418, 273

Gredel, R. 1997, A&A, 320, 929

Gregersen, E. M., & Evans, N. J. II 2000, ApJ, 538, 260

Gredel, R., Pineau des Forêts, G., & Federman, S. R. 2002, A&A, 389, 993

Gry, C., Boulanger, F., Nehmé, C., et al. 2002, A&A, 391, 675

Haikala, L. K., Harju, J., Mattila, K., & Toriseva, M. 2005, A&A, 431, 149

Heithausen, A., Bertoldi, F., & Bensch, F. 2002, A&A, 383, 591

Hily-Blant, P. 2004, Ph.D. Thesis, Université de Paris-Sud

Hily-Blant, P., & Falgarone, E. 2006, A&A, in revision (Paper II)

Hily-Blant, P., Falgarone, E., & Pety, J. 2006, in prep. (Paper IV)

Joulain, K., Falgarone, E., Pineau des Forêts, G., & Flower, D. 1998, A&A, 340, 241 (JFPF)

Lacour, S., Ziskin, V., Hébrard, G., et al. 2005, ApJ, 627, 251

Lambert, D. L., & Danks, A. C. 1986, ApJ, 303, 401

Le Petit, F., Roueff, E., & Herbst, E. 2004, A&A, 417, 993

Lee, C. W., Myers, P. C., & Tafalla, M. 2001, ApJS, 136, 703

Lis, D. C., Pety, J., Phillips, T. G., & Falgarone, E. 1996, ApJ, 463, 629

Liszt, H. S., & Lucas, R. 1994, ApJ, 431, L131

Liszt, H. S., & Lucas, R. 2000, A&A, 355, 333

Lucas, R., & Liszt, H. S. 1996, A&A, 307, 237

Lucas, R., & Liszt, H. S. 2000, A&A, 358, 1069

Moffatt, H. K., Kida, S., & Ohkitani, K. 1994, JFM, 259, 241

McCall, B. J., Huneycutt, A. J., Saykally, R. J., et al. 2003, Nature, 422, 500

Mizuno, A., Onishi, T., Yonekura, Y., et al. 1995, ApJ, 445, L161

Neufeld, D. A., Kaufman, M. J., Goldsmith, P. F., et al. 2002, ApJ, 580, 278

Pety, J., & Falgarone, E. 2000, A&A, 356, 279

Pety, J., & Falgarone, E. 2003, A&A, 412, 417

Plume, R., Kaufman, M. J., Neufeld, D. A., et al. 2004, ApJ, 605, 247

Porter, D. H., Pouquet, A., & Woodward, P. R. 1994, Phys. Fluids, 6, 2133

Tafalla, M., Mardones, M., Myers, P. C., et al. 1998, ApJ, 504, 900

Ungerechts, H., & Thaddeus, P. 1987, ApJS, 63, 645

Ward-Thompson, D., Scott, P. F., Hills, R. E., & André, P. 1994, MNRAS, 268, 276